



# A universal biomolecular integral feedback controller for robust perfect adaptation

## Journal Article

### Author(s):

[Aoki, Stephanie Kiyomi](#) ; [Lillacci, Gabriele](#); [Gupta, Ankit](#); [Baumschlager, Armin](#); [Schweingruber, David](#); [Khammash, Mustafa Hani](#) 

### Publication date:

2019-06-27

### Permanent link:

<https://doi.org/10.3929/ethz-b-000351590>

### Rights / license:

[In Copyright - Non-Commercial Use Permitted](#)

### Originally published in:

Nature 570(7762), <https://doi.org/10.1038/s41586-019-1321-1>

### Funding acknowledgement:

149802 - Quantitative in vivo characterization of RNA interference using Synthetic and Systems Biology (SNF)  
743269 - Theory and Design tools for bio-molecular control systems (EC)  
766840 - Control Engineering of Biological Systems for Reliable Synthetic Biology Applications (EC)

# A universal biomolecular integral feedback controller for robust perfect adaptation

Stephanie K. Aoki<sup>1,†</sup>, Gabriele Lillacci<sup>1,†</sup>, Ankit Gupta<sup>1,†</sup>, Armin Baumschlager<sup>1</sup>, David Schweingruber<sup>1</sup>, and Mustafa Khammash\*<sup>1</sup>

<sup>1</sup>Department of Biosystems Science and Engineering, ETH Zürich, Switzerland

<sup>†</sup>These authors contributed equally to this work.

Homeostasis is a recurring theme in biology. Homeostatic mechanisms commonly ensure that regulated variables robustly and completely adapt to environmental perturbations. This robust perfect adaptation (RPA) feature is achieved by incorporating mathematical integration in a negative feedback strategy.<sup>1,2</sup> Despite its benefits in natural circuits, the synthetic realization of integral feedback has remained elusive due to the complexity of the required biological computations. Here we first mathematically prove that there is fundamentally a single biomolecular controller topology<sup>3</sup> that realizes integral feedback for arbitrary intracellular networks with noisy dynamics. Such a topology guarantees RPA for both the cell population-average and for the time-average of single cells. We then develop the first synthetic gene network implementation of such an integral controller in a living cell,<sup>4</sup> and demonstrate its tunability and adaptation properties. A growth control application shows the inherent capacity of our integral feedback controller to deliver robustness, and highlights its potential use as a versatile controller for regulation of biological variables in uncertain networks. Our results provide new conceptual and practical tools in the area of Cybergeneetics<sup>3,5</sup> where control theory and synthetic biology come together to enable the engineering of novel synthetic controllers that steer the dynamics of living systems.<sup>3-9</sup>

Integral feedback control is arguably one of the most fundamental regulation strategies in engineering practice. From modern jetliners to industrial plants, integral feedback loops reliably drive physical variables to their desired values with great robustness and precision.<sup>10</sup> It is becoming increasingly appreciated that

nature's evolutionary explorations had already discovered the same strategy, which has functioned at various levels of biological organization to achieve homeostasis and robust adaptation to perturbations.<sup>1,2,11-13</sup> Integral feedback works by measuring the deviation of a variable of interest (*controlled variable*) from the desired target value (*set-point*), computing the mathematical integral of that deviation (*error*) over time, and then using it in a negative feedback configuration to drive processes that counteract the deviation and drive it to zero (Fig. 1a, b). Remarkably, this can be achieved despite considerable uncertainty in process dynamics and constant or slowly varying perturbations. This fundamental network property is known as *robust perfect adaptation (RPA)*, and the importance of integral feedback as a regulation strategy derives from its capacity to realize it. Given the complexity of sensing and computation (e.g. subtraction, integration, etc.) required, the *in vivo* synthetic implementation and demonstration of full integral feedback has remained unrealized. In a recent theoretical work,<sup>3</sup> we introduced the *antithetic feedback* motif (Fig. 1c) as a network topology that realizes integral feedback while lending itself to biomolecular implementation. We analytically showed that for cells with in-

\*To whom correspondence should be addressed: mustafa.khammash@bsse.ethz.ch

trinsically noisy dynamics, this regulatory motif endows the network with guaranteed robustness properties for the population-average and also for the single-cell time-average. In fact this motif subtly exploits intrinsic noise to use it as a stabilization force in scenarios when noise-free dynamics exhibit oscillations.

Consider the problem of controlling an uncertain and noisy biomolecular network by augmenting it with another feedback controller network (see the *Theory Box*, top-left figure). The control objective is to achieve RPA for some variable in the controlled network (output) i.e. this variable must be steered to a desired set-point and maintained there, even in the presence of unknown constant external perturbations and in spite of uncertainty in the network topology and parameters, including the parameters of the controller network. Insisting on robustness to topology and parameters is particularly important in synthetic biology where the controlled network is often unknown or poorly characterized, and fine-tuning the parameters of the controller network can be extremely difficult.

It is well-established in control theory<sup>14,15</sup> that in the noise-free setting such general purpose controller networks need to implement an integral feedback component, but designing them is challenging because of the realizability and other constraints imposed by biomolecular reaction network.<sup>16,17</sup> These challenges are further amplified if one takes into account the noisy nature of the intracellular dynamics, where not all integral feedback controller implementations lead to RPA, and hence the particular topology used is critical. In this stochastic setting, when the dynamics is stable RPA refers to the steady-state population average of the output variable, or equivalently its long-term single-cell time average.

Given this context, there are several fundamental questions that arise naturally. How can one determine definitively whether a candidate network of any size

achieves RPA in the presence of intrinsic noise? What architectural features are necessary and sufficient for a biomolecular feedback control topology to achieve RPA? Can all RPA achieving controller topologies, regardless of their size, be characterized? If the number of species needed to implement a controller topology is used as a measure of its complexity, what controller topologies achieve RPA with minimal complexity? Here we provide definitive answers to all these questions. We prove that each RPA-achieving controller must necessarily embed the antithetic feedback motif and hence the antithetic feedback motif we introduced previously<sup>3</sup> is the minimal complexity RPA-achieving controller for unknown networks with noisy dynamics. It is important to emphasize that these results *only* hold in the setting of noisy single-cell dynamics. If the network under consideration is noise-free, it is not necessary for a controller to embed antithetic feedback for achieving RPA<sup>18–21</sup> but it is sufficient. These results are summarized in the *Theory Box* and their detailed proofs are in the Supplementary Text.

The original analysis of the antithetic feedback controller<sup>3</sup> was focused on the ideal case in which the production rates of the molecular species involved in the circuit are unsaturated, and there is negligible degradation of controller proteins  $Z_1$  and  $Z_2$ . In living cells, these assumptions are not satisfied due to the fact that all genes have a limited production capacity, and in the case of fast-growing cells, dilution of the controller proteins must be factored into the dynamics.<sup>16</sup> This can introduce an error between the actual and desired values of the controlled variable following a large disturbance. To investigate whether this error could be made small enough, we simulated a model of the antithetic motif in an *E. coli* implementation (Supplementary Text, Section S1, Extended Data Figs. 1, 2). Our analysis revealed that using realistic model parameters it is

indeed possible to achieve small errors, suggesting that for all practical purposes the antithetic motif can realize perfect adaptation in growing cells.

Central to our implementation of the minimal antithetic design<sup>3,4</sup> are two controller proteins that “annihilate” (or stoichiometrically inactivate) each other, for example by forming an inert dimer (Fig. 1c). Such an annihilation reaction has been used in existing synthetic devices,<sup>6,22</sup> and to realize it we used a previously reported pair of *Bacillus subtilis*  $\sigma$  and anti- $\sigma$  factors, SigW and RsiW, which play a role in cell envelope homeostasis and has been shown to display annihilation *in vivo*.<sup>22,23</sup> In its natural context, RsiW stably sequesters and holds SigW inactive.<sup>23</sup> Upon cell membrane stress, RsiW is proteolytically cleaved and active SigW is released, controlling expression of multiple downstream genes.<sup>23</sup> The high native stability of this  $\sigma$  and anti- $\sigma$  factor enables practical realization of integral action in fast growing cells, in contrast to RNA-based controllers<sup>5,8,9</sup> where RNA instability poses a major limitation to integral action realization.

In our setup, on one plasmid SigW-responsive promoter  $P_{\text{sigW}}$  drives the controlled genes, *E. coli* transcription factor *araC* and *sfgfp* (superfolder green fluorescent protein). AraC closes the loop by regulating  $P_{\text{BAD}}$  promoter-driven *rsiW* expression in a concentration-dependent manner (Fig. 2a). sfGFP should be proportional to AraC, the regulated protein of interest. To mitigate saturation effects, the final plasmid contains two  $P_{\text{sigW-araC-sfgfp}}$  modules (Supplementary Text, Fig. 2a, Extended Data Fig. 2). This circuit is tunable with arabinose (ARA), which increases AraC activity, and N-(3-oxohexanoyl)-L-homoserine lactone (HSL), which activates constitutively-expressed *Vibrio fischeri* quorum sensing pathway transcription factor LuxR to induce *sigW* expression driven by *lux* promoter ( $P_{\text{LUX}}$ ). For comparison, an open-loop control

circuit was constructed without  $P_{\text{BAD-rsiW}}$  to disable feedback (Fig. 2b).

Testing of the closed-loop circuit shows that steady-state *sfgfp* levels can be adjusted with ARA and HSL by independently tuning *sigW* and *rsiW* expression (Fig. 2c), consistent with our theory and with recent work.<sup>3,24</sup> Increasing SigW production resulted in a corresponding increase in steady-state sfGFP between 0 and 10 nM HSL, whereas increasing RsiW production between 0.05% and 0.2% arabinose corresponded to a sfGFP decrease. Dynamic time courses of closed-loop cells pre-cultured in ARA and induced with HSL show unimodal fluorescence detectable over background and stable over long periods of time (Fig. 2d, Extended Data Fig. 3). Further, using cell growth rate as a burden indicator,<sup>7</sup> in the conditions tested differences in growth rates between set-points or over time were insignificant (Extended Data Fig. 4).

To test the system’s response to a constant perturbation, on a separate plasmid we used the orthogonal *Mesoplasma florum* protease *mf-Lon*<sup>25</sup> driven by an anhydrotetracycline (aTc) inducible promoter ( $P_{\text{TET}}$ , Fig. 2a, b). *mf-Lon* recognizes cognate Pdt degradation tags<sup>25</sup> appended to the C-termini of AraC and sfGFP and increases protein degradation (Methods, Extended Data Fig. 5). Steady-state sfGFP levels of both circuits with and without *mf-Lon* induction were measured and disturbance rejection was quantified as the relative output decrease post-disturbance. For multiple ARA and HSL conditions, the closed-loop showed virtually no change in fluorescence after protease induction, while the open-loop showed greater than 40% decrease in most conditions tested and neither circuit showed significant burden due to protease induction (Fig. 2e, Extended Data Fig. 4). Dynamically, the closed-loop adapts post-perturbation after a short transient (Fig. 2f, Extended Data Fig. 4). These results suggest that the

closed-loop is able to sense and compensate for AraC loss despite the continued presence of the perturbation, unlike the open-loop. We further found that adaptation was maintained when decreasing HSL, increasing arabinose, or increasing both HSL and arabinose from these conditions (Extended Data Fig. 6). However, increasing HSL and reducing arabinose eventually leads to discernible error (though always smaller than the open-loop error), indicating an exit from the adaptation region, as qualitatively predicted by the simulations (Extended Data Fig. 6). The observed conditions where perfect adaptation to the *mf*-Lon disturbance is achieved is limited to an approximate three-fold output range (Extended Data Fig. 6), although the closed-loop circuit is capable of reaching higher set-points in the absence of this disturbance. Moreover, the closed-loop tended to show increased cell-to-cell variability compared to the open-loop and showed decreased cell-to-cell variability upon perturbation, consistent with theoretical analyses<sup>26</sup> (Extended Data Fig. 7).

To demonstrate the application potential of our integral feedback controller and its inherent capacity to confer robustness, the closed- and open-loop circuits were modified to regulate cell growth rate by exchanging *sfgfp* for *metE* (methionine synthase, Fig. 3a, b). Methionine is required for cell viability and biomass accumulation. In a host strain deleted for endogenous *metE*, cell growth can be controlled in methionine-free medium through regulation of *metE* expression (Fig. 3a, b).<sup>27</sup> The closed-loop growth rate is tunable with HSL in cultures grown in fixed ARA (Fig. 3c, Extended Data Fig. 8). Furthermore, when a constant environmental perturbation was applied by changing cell incubation temperature from 37°C to 30°C (Fig. 3d, left panel), the closed-loop induced with 10 nM HSL and 0.2% ARA maintained its growth rate. In contrast, the open-loop growth slowed significantly at the lower temperature

(Fig. 3d, right panel, Extended Data Fig. 8), suggesting that the perturbation in the closed-loop strain at this set-point is compensated for at 30°C through *metE* regulation. Given that the set-point is determined ratiometrically by SigW and RsiW, within the region of adaptation any such global perturbation (e.g. extrinsic noise) that affects their expression in a similar way should also be rejected by the controller.

Robust perfect adaptation (RPA) is exhibited by many endogenous biological systems,<sup>2,12,28</sup> and understanding which network topologies allow RPA is of fundamental importance. This work is different from existing studies on this phenomenon<sup>19–21</sup> in two distinct ways. First we study adaptation in the stochastic setting where the effects of intrinsic biochemical noise<sup>29</sup> are incorporated. Second we address scenarios when the controlled network has unknown players or interactions. We separate the “controller network” from the “controlled network” (see the *Theory Box*) and allow the latter to be completely arbitrary while the former can have uncertain parameters. In this setting, our mathematical analysis proves that the integral feedback action necessary for RPA, can *only* be exactly implemented with biomolecular reactions by a controller that embeds the antithetic feedback controller topology. Remarkably this controller topology is known to enhance intrinsic noise and cell-to-cell heterogeneity,<sup>26,30</sup> yet it plays a universal role in ensuring RPA for the population-average (or the single-cell time-average) for arbitrary intracellular networks. It is worth remarking that the antithetic topology has been recently found in several endogenous pathways.<sup>3,31</sup>

The rationally-designed integral controller reported here presents a proof of concept design that establishes the feasibility to engineer robust homeostasis in synthetic biology. A suitably optimized version of this controller with expanded dynamic range should find wide application in all scenarios in which protein expression

must remain tightly regulated at the desired level, independent of other intervening processes. In metabolic engineering, for instance, robust set-point regulation of key enzymes could be used to redirect metabolic fluxes to maximize yield and minimize host toxicity. Probing endogenous pathways could also benefit from such regulation, because compensatory cellular mechanisms tend to alter expression in complex ways. A mammalian analog of our synthetic integral feedback module could also offer exciting perspectives for cell therapy in all those conditions that result from dysregulation of homeostasis, by enabling the implementation of a fully autonomous and personalized intervention.

## Acknowledgments

We thank T. Frei, C. Briat, D. Meyer and G. Schmidt for assistance with the project. This project has received funding from the Swiss National Science Foundation (31003A-149802), the European Research Council (ERC) under the European Union's Horizon 2020 research and innovation programme (CyberGenetics; grant agreement 743269), and from the European Union's Horizon 2020 research and innovation programme (COSY-BIO; grant agreement 766840).

## Author Contribution

M.K., G.L., and S.K.A. conceived the project and designed the circuit. S.K.A., G.L., and D.S. constructed the circuits. G.L. performed the computational modeling. A.G. proved the theoretical results. S.K.A., G.L., and A.B. planned and performed the experiments and data analysis. All authors wrote the manuscript.

## Author Information

Reprints and permissions information is available at [www.nature.com/reprints](http://www.nature.com/reprints). The authors declare no competing interests. Correspondence and requests for materials should be addressed to [mustafa.khammash@bsse.ethz.ch](mailto:mustafa.khammash@bsse.ethz.ch).

## Supplementary materials

Supplementary Text  
Supplementary Figure 1  
Tables S1 and S2

## References

- [1] Yi, T.-M., Huang, Y., Simon, M. I. & Doyle, J. Robust perfect adaptation in bacterial chemotaxis through integral feedback control. *Proceedings of the National Academy of Sciences* **97**, 4649–4653 (2000).
- [2] El-Samad, H., Goff, J. & Khammash, M. Calcium homeostasis and parturient hypocalcemia: an integral feedback perspective. *Journal of Theoretical Biology* **214**, 17–29 (2002).
- [3] Briat, C., Gupta, A. & Khammash, M. Antithetic integral feedback ensures robust perfect adaptation in noisy biomolecular networks. *Cell systems* **2**, 15–26 (2016).
- [4] Lillacci, G., Aoki, S. K., Schweingruber, D. & Khammash, M. A synthetic integral feedback controller for robust tunable regulation in bacteria. *bioRxiv* (2017).
- [5] Lillacci, G., Benenson, Y. & Khammash, M. Synthetic control systems for high performance gene expression in mammalian cells. *Nucleic acids research* **46**, 9855–9863 (2018).
- [6] Hsiao, V., de los Santos, E. L., Whitaker, W. R., Dueber, J. E. & Murray, R. M. Design and implementation of a biomolecular concentration tracker. *ACS synthetic biology* **4**, 150–161 (2014).
- [7] Ceroni, F. *et al.* Burden-driven feedback control of gene expression. *Nature methods* **15**, 387 (2018).

- [8] Huang, H.-H., Qian, Y. & Del Vecchio, D. A quasi-integral controller for adaptation of genetic modules to variable ribosome demand. *Nature Communications* **9**, 5415 (2018).
- [9] Kelly, C. L. *et al.* Synthetic negative feedback circuits using engineered small rnas. *Nucleic acids research* **46**, 9875–9889 (2018).
- [10] Åström, K. J. & Murray, R. M. *Feedback systems: an introduction for scientists and engineers* (Princeton university press, 2010).
- [11] Miller, P. & Wang, X.-J. Inhibitory control by an integral feedback signal in prefrontal cortex: a model of discrimination between sequential stimuli. *Proceedings of the National Academy of Sciences of the United States of America* **103**, 201–206 (2006).
- [12] Muzzey, D., Gómez-Urbe, C. A., Mettetal, J. T. & van Oudenaarden, A. A systems-level analysis of perfect adaptation in yeast osmoregulation. *Cell* **138**, 160–171 (2009).
- [13] Ben-Zvi, D. & Barkai, N. Scaling of morphogen gradients by an expansion-repression integral feedback control. *Proceedings of the National Academy of Sciences* **107**, 6924–6929 (2010).
- [14] Francis, B. A. & Wonham, W. M. The internal model principle of control theory. *Automatica* **12**, 457–465 (1976).
- [15] Sontag, E. D. Adaptation and regulation with signal detection implies internal model. *Systems & control letters* **50**, 119–126 (2003).
- [16] Ang, J., Bagh, S., Ingalls, B. P. & McMillen, D. R. Considerations for using integral feedback control to construct a perfectly adapting synthetic gene network. *Journal of theoretical biology* **266**, 723–738 (2010).
- [17] Xiao, F. & Doyle, J. C. Robust perfect adaptation in biomolecular reaction networks. *bioRxiv* 299057 (2018).
- [18] Briat, C., Zechner, C. & Khammash, M. Design of a synthetic integral feedback circuit: dynamic analysis and dna implementation. *ACS synthetic biology* **5**, 1108–1116 (2016).
- [19] Ma, W., Trusina, A., El-Samad, H., Lim, W. A. & Tang, C. Defining network topologies that can achieve biochemical adaptation. *Cell* **138**, 760–773 (2009).
- [20] Tang, Z. F. & McMillen, D. R. Design principles for the analysis and construction of robustly homeostatic biological networks. *Journal of theoretical biology* **408**, 274–289 (2016).
- [21] Araujo, R. P. & Liotta, L. A. The topological requirements for robust perfect adaptation in networks of any size. *Nature communications* **9**, 1757 (2018).
- [22] Chen, D. & Arkin, A. P. Sequestration-based bistability enables tuning of the switching boundaries and design of a latch. *Molecular systems biology* **8**, 620 (2012).
- [23] Helmann, J. D. Bacillus subtilis extracytoplasmic function (ecf) sigma factors and defense of the cell envelope. *Current opinion in microbiology* **30**, 122–132 (2016).
- [24] Annunziata, F. *et al.* An orthogonal multi-input integration system to control gene expression in escherichia coli. *ACS Synthetic Biology* (2017).
- [25] Ewen Cameron, D. & Collins, J. J. Tunable protein degradation in bacteria. *Nat. Biotechnol.* **32**, 1276–1281 (2014).
- [26] Briat, C., Gupta, A. & Khammash, M. Antithetic proportional-integral feedback for reduced variance and improved control performance of stochastic reaction networks. *Journal of The Royal Society Interface* **15**, 20180079 (2018).
- [27] Miliadis-Argeitis, A., Rullan, M., Aoki, S. K., Buchmann, P. & Khammash, M. Automated optogenetic feedback control for precise and robust regulation of gene expression and cell growth. *Nature Communications* **7** (2016).
- [28] Barkai, N. & Leibler, S. Robustness in simple biochemical networks. *Nature* **387**, 913 (1997).
- [29] Elowitz, M. B., Levine, A. J., Siggia, E. D. & Swain, P. S. Stochastic gene expression in a single cell. *Science (New York, N.Y.)* **297**, 1183–6 (2002).
- [30] Hilfinger, A., Norman, T. M., Vinnicombe, G. & Paulsson, J. Constraints on fluctuations in sparsely characterized biological systems. *Physical review letters* **116**, 058101 (2016).
- [31] Ferrell, J. E. Perfect and near-perfect adaptation in cell signaling. *Cell systems* **2**, 62–67 (2016).
- [32] Chung, C. T., Niemela, S. L. & Miller, R. H. One-step preparation of competent escherichia coli: transformation and storage of bacterial cells in the same solution. *Proc. Natl. Acad. Sci. U. S. A.* **86**, 2172–2175 (1989).
- [33] Pédelacq, J.-D., Cabantous, S., Tran, T., Terwilliger, T. C. & Waldo, G. S. Engineering and characterization of a superfolder green fluorescent protein. *Nature biotechnology* **24**, 79–88 (2006).

## Figure legends



**Theory Box: Universality of the antithetic feedback controller motif**

Consider the problem of controlling an arbitrary biomolecular network, comprising species  $\mathbf{X}_1, \dots, \mathbf{X}_N$ , by connecting it with a feedback controller that is realizable as another network with species  $\mathbf{Z}_1, \dots, \mathbf{Z}_C$  (*top-left* figure). The controlled network species can interact with the controller species via *actuation* reactions that do not affect the controller’s state, and via a *sensing* reaction, that is catalyzed by the output species of interest  $\mathbf{X}_\ell$  and acts by producing/degrading some controller species  $\mathbf{Z}_i$  (e.g.  $\mathbf{Z}_i + \mathbf{X}_\ell \rightarrow \mathbf{X}_\ell$  or  $\mathbf{X}_\ell \rightarrow \mathbf{Z}_i + \mathbf{X}_\ell$ ). Additionally there is a *set-point encoding* reaction that can produce/degrade some controller species  $\mathbf{Z}_j$ . The set-point encoding reaction and the sensing reaction follow mass-action kinetics with positive rate-constants  $\mu$  and  $\theta$  respectively. The sensed variable is the abundance of  $\mathbf{X}_\ell$  scaled multiplicatively by  $\theta$ , and our control objective is to robustly steer its average value to the desired set-point  $\mu$ . Excluding the set-point encoding and sensing reactions, we assume that each of the remaining closed-loop network reactions depend on at least one parameter in the vector of parameters denoted by  $\gamma = (\gamma_1, \gamma_2, \dots)$ . To capture the effects of intrinsic noise, we model the reaction dynamics as a *continuous-time Markov chain* (CTMC)  $(X_\gamma(t), Z_\gamma(t))_{t \geq 0}$ . A single-cell’s output at time  $t$  is the random state  $X_{\gamma, \ell}(t)$  denoting the copy-number of the output species  $\mathbf{X}_\ell$ , while the *population-averaged* output of several identical cells is given by the expectation  $\mathbb{E}(X_{\gamma, \ell}(t))$ . The controller’s goal is to achieve RPA for the population-average by ensuring that  $\lim_{t \rightarrow \infty} \mathbb{E}(\theta X_{\gamma, \ell}(t)) = \mu$  holds, regardless of the initial conditions and the parameter vector  $\gamma$ . In other words, the population-average adapts perfectly following a state-perturbation or after a disturbance that alters one or more of the parameters in  $\gamma$ . This property also holds for the long-term average output of a single cell given by  $\lim_{T \rightarrow \infty} T^{-1}(\int_0^T \theta X_{\gamma, \ell}(t) dt)$ . We prove that all RPA-achieving controllers must have at least two species (i.e.  $C \geq 2$ ), and that the species involved in set-point encoding (say  $\mathbf{Z}_1$ ) and output sensing (say  $\mathbf{Z}_2$ ) must be distinct. We further find a linear-algebraic condition that provides a remarkably simple parametrization of all feedback controllers of any size that achieve RPA (Supplementary Text, Theorem S2.5). This condition can be further unraveled to prove that each RPA-achieving controller must embed an antithetic motif. Specifically the species-set of any RPA controller can be partitioned into three disjoint subsets  $\mathcal{C}_+$ ,  $\mathcal{C}_-$  and  $\mathcal{C}_0$  (*top-right* figure), containing species  $\mathbf{Z}_1$ ,  $\mathbf{Z}_2$  and the null species  $\emptyset$  respectively, and there must exist an annihilation reaction that combines a species in  $\mathcal{C}_+$  with one in  $\mathcal{C}_-$  to produce a species in  $\mathcal{C}_0$  (shown with thick red arrows above). Hence, any RPA-achieving controller can be viewed as an extension of the minimal antithetic feedback controller presented in<sup>3</sup> (Supplementary Text, Section S2.2.3). Moreover it can be shown that the class of RPA-achieving controllers in the stochastic setting is strictly contained in the class of such controllers in the deterministic setting, where the population-averaged dynamics coincides with the single-cell dynamics (Supplementary Text, Section S2.2.4).

Figure 1: **Integral feedback enables robust perfect adaptation.** (a) In a circuit without feedback regulation (open-loop), the output is sensitive to external perturbations, driving it away from its desired value (no adaptation). (b) Integral feedback confers robustness to perturbations and keeps the output tightly regulated at desired levels (robust perfect adaptation). (c) The antithetic integral control motif offers a biologically realizable integral feedback scheme using two regulator species. The output of interest,  $X_I$ , is sensed by a reaction whose product,  $Z_2$ , is produced at a rate proportional to  $X_I$  (rate constant  $\theta$ ). A second reference reaction yields  $Z_1$  at a rate  $\mu$ .  $Z_1$  and  $Z_2$  annihilate/sequester each other, an operation that is central to the integral feedback computation. In turn,  $Z_1$  works as an actuator by affecting processes that lead to the increase in the production of the output of interest, thereby closing the feedback loop. In this scheme, as long as the closed dynamics is stable, the steady-state value of the output is determined solely by the ratio  $\mu/\theta$ . Importantly, it does not depend on the topology and parameters of the circuit of interest, which are usually uncertain and noisy, nor on any constant external perturbations that afflict the network.

Figure 2: **Synthetic antithetic integral feedback control circuit.** (a) Closed-loop circuit. The antithetic control system (beige shaded box) is tunable with HSL and ARA. The controlled circuit of interest (gray shaded box) consists of *araC* and *sfGFP* tagged with *mf*-Lon degradation tags. A negative perturbation is applied by aTc-induction of *mflon* expression, resulting in AraC and sfGFP degradation. (b) Open-loop circuit. Closed-loop feedback is disabled by deleting the anti-sigma module ( $P_{BAD-rsiW}$ ). (c) Response of closed-loop circuit to HSL and ARA. Heatmap of the mean steady-state sfGFP fluorescence for corresponding concentrations of HSL and ARA normalized to the maximum output for four independent biological replicates. (d) Dynamic response of closed-loop circuit to HSL induction. sfGFP fluorescence is plotted as a function of time and fit with a cubic spline. Data show mean (green circles)  $\pm$  s.d. for  $n = 3$  independent biological replicates (gray circles). (e) Output steady-states of closed- and open-loop circuits in the presence of *mf*-Lon protease perturbation. sfGFP fluorescence normalized to the pre-disturbance level for each set of induction conditions. Data show mean  $\pm$  s.d. for  $n = 3$  independent biological replicates (gray circles). Two-tailed, unpaired, unequal variance t-test. Non-normalized data is available in Extended Data Fig. 6b. (f) Dynamic response of closed-loop circuit to perturbation. Closed- and open-loop strains at steady-state in 0.2% ARA and 5.5 nM HSL were perturbed at 1.5 hours by aTc-induction of *mf*-Lon expression. sfGFP fluorescence normalized to the mean at 0 hours is plotted as a function of time and fit with a cubic spline for  $n = 3$  independent biological replicates. Shaded regions indicate the s.d.. Non-normalized data is available in Extended Data Fig. 6f.

Figure 3: **Growth rate control.** **(a)** Closed-loop antithetic integral feedback control of growth rate. The antithetic controller (beige shaded box) controls the circuit of interest (gray shaded box), in which *sfgfp* was replaced with *metE*. MetE catalyzes the last step of cobalamin-independent methionine (met) biosynthesis by transferring a methyl group from 5-methyltetrahydropteroyl-tri-L-glutamate to L-homocysteine (hcy, blue shaded box). **(b)** Open-loop growth control circuit. Feedback is disabled by deleting the anti-sigma module ( $P_{BAD-rsiW}$ ) from the closed-loop circuit. **(c)** Growth rate is tunable in methionine-free medium. Steady-state growth rates of the closed-loop circuit in a  $\Delta metE$  host strain for the corresponding concentrations of HSL and 0.2% ARA ( $n = 3$ ). **(d)** Robustness to an external perturbation. Left: A constant external change in temperature is exerted on the closed-loop circuit strain. Right: Steady-state growth rates of closed- and open-loop circuits in a  $\Delta metE$  host strain grown at 37°C and 30°C in methionine-free medium containing 0.2% ARA and 10 nM HSL normalized to the 37°C rate for each circuit ( $n = 3$ ). Two-tailed, unpaired, unequal variance t-test. Non-normalized data is available in Extended Data Figs. 8a, b. Data show mean  $\pm$  s.d. for  $n$  independent biological replicates (gray circles, **c**, **d**). The response of the circuit to temperature perturbation at the higher set-points in **(c)** was not characterized in this study.

## Methods

### Growth conditions

Cells were grown in 14 mL tubes (Greiner) in LB (1% tryptone, 0.5% yeast extract, 1% NaCl) or M9 medium supplemented with 0.2% casamino acids, 0.45% LB, 0.4% glucose, 0.001% thiamine, 0.00006% ferric citrate, 0.1 mM calcium chloride, 1 mM magnesium sulfate, and 20  $\mu\text{g}/\text{mL}$  uracil (Sigma-Aldrich Chemie GmbH), and incubated in an environmental shaker (Excella E24, New Brunswick) at 37°C with shaking at 230 rpm unless otherwise indicated. Antibiotics (Sigma-Aldrich Chemie GmbH) were used at the following concentrations: chloramphenicol (cam), 34  $\mu\text{g}/\text{mL}$ ; spectinomycin (spec), 100  $\mu\text{g}/\text{mL}$ ; ampicillin (amp), 100  $\mu\text{g}/\text{mL}$ ; kanamycin (kan), 40  $\mu\text{g}/\text{mL}$ . Arabinose was received from Sigma-Aldrich Chemie GmbH. N-(3-oxo-hexanoyl)-L-homoserine lactone (HSL) and anhydrotetracycline (aTc) were received from Chemie Brunschwig AG. For all experiments, growth medium containing HSL was stored at 4°C for the duration of the experiment and prewarmed to 37°C 30 minutes before use to minimize degradation of the inducer.

### Host strain and plasmids construction

Restriction enzymes, T4 DNA ligase and Taq ligase used in this study were purchased from New England Biolabs. Herculase II Fusion DNA Polymerase (Agilent) and Phusion Polymerase (New England Biolabs) were used for cloning polymerase chain reactions (PCR). T5 exonuclease was purchased from Epicentre. DNA isolation was performed using ZR Miniprep Classic, DNA Clean and Concentrator, and Zymoclean Gel DNA Recovery Kits (Zymo Research). DNA oligonucleotide primers were synthesized by Sigma-Aldrich Chemie GmbH, Integrated

DNA Technologies, and Microsynth AG. Sequences of all plasmid and strain constructs were confirmed by Microsynth AG. DNA was transformed into cells as previously described.<sup>32</sup> All strains, plasmids, and primers used in this study are listed in Supplementary Tables S1 and S2. Plasmid maps are presented in Extended Data Figs. 9 and 10. Strains and plasmids were constructed using standard cloning methods. Construction details are described in section S3 of the Supplementary Text.

### Strain and plasmids used for fluorescence studies

The host strain MG1655  $\Delta\text{araCBAD}$   $\Delta\text{lacIZYA}$   $\Delta\text{araE}$   $\Delta\text{araFGH}$   $\text{attB}::\text{lacYA177C}$   $\Delta\text{rhaSRT}$   $\Delta\text{rhaBADM}$   $\text{Tn7}::\text{tetR}$ , referred to as SKA703, was used for all sfGFP<sup>33</sup> circuits in this study.

The negative perturbation plasmid (pSKA417, Genbank accession #MK775703) used in these studies was constructed by placing the *Mesoplasma florum* Lon protease gene *mflon*<sup>25</sup> under a TetR-repressible promoter ( $P_{\text{TET}}$ ) on a medium copy plasmid with a p15A origin of replication and spectinomycin-resistance (Extended Data Fig. 10a.).

The closed- and open-loop plasmids used in this study were modularly constructed on a high copy plasmid with ColE1 origin of replication and ampicillin-resistance. Initially, a closed-loop precursor plasmid (pSKA538, Genbank accession #MK775704) was built, consisting of  $P_{\text{sigW-sRBS-V5}}::\text{araC}::\text{pdt}\#3\text{-FLAG}::\text{sfgfp}::\text{pdt}\#1$ ,  $\text{luxR-}P_{\text{LUX-RBS5000-sigW}}$ , and  $P_{\text{BAD-RBS5000-rsiW}}$ . (Extended Data Fig. 10b). An open-loop variant precursor plasmid (pSKA539, Genbank accession #MK775705) was also constructed with feedback disabled by removing the  $P_{\text{BAD-RBS5000-rsiW}}$  module (Extended Data Fig. 10b). The final versions of the circuits used in this study (pSKA562 and pSKA563,

Genbank accession #MK775706 and MK775707) were constructed by adding a second tandem copy of *P<sub>sigW-sRBS-V5::araC::pdt#3c-FLAG::sfgfp::pdt#1</sub>* to each plasmid (Extended Data Fig. 10c).

## Strains and plasmids used for growth rate control studies

A variant of SKA703 (SKA1328) with endogenous *metE* deleted was used for all growth rate control experiments.

Closed-loop growth rate control plasmid pSKA570 (Genbank accession #MK775708) and open-loop growth rate control plasmid pSKA571 (Genbank accession #MK775709) were constructed by exchanging *sfgfp* for *metE* with a weak ribosomal binding site (Extended Data Fig. 10d). Open-loop variant pSKA571-p15A (Genbank accession #MK775710) is identical to pSKA571 but with a lower-copy p15A origin of replication. (Extended Data Fig. 10d).

## V5-AraC-Pdt#3c immunoblot

During the course of this study it was observed that the efficiency of *mf*-Lon protease-dependent degradation was not only affected by the degradation tag sequence but also by the tagged protein itself. Originally, a Pdt#1 degradation tag was used for both AraC and sfGFP. However, immunoblot analysis of V5-AraC-Pdt#1 suggested that AraC was being more efficiently degraded by the *mf*-Lon protease than sfGFP (data not shown). Changing the AraC degradation tag from Pdt#1 to the weaker Pdt#3c tag resulted in an improvement in matching sfGFP degradation rates (Extended Data Fig. 5).

SKA703 pSKA417 pSKA539 (open-loop, *V5::araC::pdt#3c*, *FLAG::sfgfp::pdt#1*) was grown overnight in 5 mL M9-0.2% arabinose and appropriate

antibiotics. SKA703 (no plasmid negative control strain) was grown overnight in 5 mL M9-0.2% arabinose (antibiotic-free). The overnight cultures were diluted into 5 mL aliquots of M9-0.2% arabinose and appropriate antibiotics containing 5 nM HSL with or without 10 ng/mL aTc at a low optical density (OD, 0.00008 starting OD for SKA703 pSKA417 pSKA539; 0.00004 starting OD for negative control SKA703), and incubated for 4.5 hours before being rediluted into 5 mL aliquots of prewarmed matching media at low OD (SKA703 pSKA417 pSKA539 at 0.00004 OD; SKA703 at 0.00001 OD) followed by another 4.5 hours of incubation.

After 9 hours of induction, culture samples were measured in triplicate for sfGFP fluorescence by flow cytometry. 4.5 mL aliquots of each culture were pelleted at 4°C. Cell pellets were resuspended in 1X lysis buffer (1X BugBuster (Merck and Cie), 1X cComplete EDTA-free Protease Inhibitor (Roche Diagnostics Schweiz AG), 60 mM Tris-HCl pH 6.8 (Sigma-Aldrich Chemie GmbH), 10% glycerol (Axon Lab AG), 2% SDS (Sigma-Aldrich Chemie GmbH), 5%  $\beta$ -mercaptoethanol (Sigma-Aldrich Chemie GmbH), 1 mM phenylmethylsulfonyl fluoride (Sigma-Aldrich Chemie GmbH). Lysis buffer volume was calculated as OD  $\times$  4500  $\mu$ L/5 for all cultures. Cells were lysed at 95°C for 10 minutes and used immediately after preparation.

10  $\mu$ L aliquots of freshly prepared lysates and 0.75  $\mu$ L Odyssey Protein Marker (Li-Cor GmbH) were run on a NuPAGE 4-12% Bis-Tris mini gel (1 mm, 15 well, Invitrogen) with NuPAGE MES SDS Running Buffer (Invitrogen) at 200 V for 40 minutes under denaturing conditions.

Proteins were transferred to Immobilon-FL PVDF membrane (Merck and Cie) using NuPAGE Tris-glycine-10% methanol transfer buffer (Invitrogen) at 30 V for one hour (XCell II Blot Module, Invitrogen). The mem-

brane was dried overnight post-transfer.

The dried membrane was reactivated in methanol before being washed with water and stained for total protein using REVERT Total Protein Stain (Li-Cor) as recommended by the manufacturer. The stained membrane was imaged immediately in the 700 channel with a Li-Cor Odyssey CLx equipped with Image Studio 2.1.10 software (169  $\mu\text{m}$  resolution, medium quality, auto intensity).

After imaging, the membrane was rinsed with water and then blocked one hour at room temperature in Li-Cor Odyssey Blocking Buffer(PBS). The membrane was incubated with 1:5,000 mouse  $\alpha$ -V5 antibody [E10] (AB53418, Abcam) in blocking buffer with 0.1% Tween-20 (Sigma-Aldrich Chemie GmbH) at room temperature for one hour before being washed five times with phosphate-buffered saline (PBS)-0.1% Tween-20, five minutes each wash, followed by a one hour room-temperature secondary antibody incubation (1:10,000 Li-Cor Goat  $\alpha$ -mouse IRDye800CW 925-32210) in blocking buffer with 0.1% Tween-20. The membranes was washed five times with PBS-0.1% Tween-20, twice with PBS (no Tween-20), and scanned on a Li-Cor Odyssey CLx (700 and 800 channels, 169  $\mu\text{m}$  resolution, medium quality, auto intensity).

Densitometry analysis of the total protein and V5 band intensities were analyzed using Li-Cor Image Studio 2.1.10 software. Background subtraction was performed using median pixel values and a border width of 3. All lanes were within the linear detection range of both the REVERT Total Protein Stain and V5 antibody staining with the exception of the SKA703 negative control, which was below the linear detection range for V5 signal (data not shown). The V5 immunoblot signal was normalized to the total detected protein for each lane.

## High throughput ARA and HSL titrations

All titration assays to measure the response of closed-loop circuit strain SKA703 pSKA417 pSKA562 to different inducer concentrations were performed on a Tecan EVO 200 robotic platform in 96-well plates (NUNC). For each biological replicate, an independent master culture was grown at 37°C with shaking for a minimum of 12 hours to stationary phase in M9 medium with 0.2% arabinose and antibiotics. The final volume of each well was 150  $\mu\text{L}$ . To start the experiment, the master culture was diluted 1:10,000 in individual wells at 4°C containing M9 minimal medium with antibiotics and the desired combinations of inducers (HSL and arabinose). Each biological replicate was cultured in medium prepared independently from the other replicates. This first dilution was incubated at 37°C for 6 hours, and then diluted again 1:10,000 in a fresh plate at 4°C, with each well being diluted into the corresponding well of the new plate (to maintain the same inducer concentrations). The second dilution was incubated at 37°C for 5 hours, after which the plate was analyzed at room temperature with flow cytometry. The reported data are from four independent biological replicates pooled from experiments performed on two separate days.

## Step responses

5 mL aliquots of M9 media with appropriate antibiotics and 0.15% or 0.2% arabinose were inoculated with SKA703 pSKA417 pSKA562 (closed-loop) from glycerol freeze stocks at an OD of  $8 \times 10^{-8}$ . The cultures were incubated for 9 hours overnight at 37°C with shaking. In the morning, the overnight cultures were in early logarithmic phase. The overnight cultures were diluted into 5 mL fresh prewarmed induction media at 0.005 OD and

incubated at 37°C with shaking. The 0.15% overnight arabinose cultures were diluted into media containing 0.15% arabinose and 5 nM HSL. The 0.2% overnight arabinose cultures were diluted into media containing 0.2% arabinose and either 5.5 nM, 7.5 nM or 8.5 nM HSL. Every 1.5 hours, ODs were measured and all cultures were rediluted into matching prewarmed induction media at 0.005 OD. At every dilution point, three 200  $\mu$ L samples of culture were collected and measured by flow cytometry and the average of the technical replicates were used. ODs were used to calculate cell growth rate. The reported data are from three independent biological replicates pooled from experiments performed on the same day. For each biological replicate, a separate stock of media was independently prepared and used only for that particular replicate. Every biological replicate was started from its own independently-prepared overnight culture.

### Induction of negative perturbation

SKA703 pSKA417 pSKA562 (closed-loop) and SKA703 pSKA417 pSKA563 (open-loop) strains were grown overnight in M9 medium containing 0.1%, 0.15%, and 0.2% arabinose. Overnight cultures were diluted into fresh media with matching arabinose concentrations and different concentrations of HSL (3.5 and 4 nM HSL with 0.1% arabinose, 5, 5.5, and 7 nM HSL with 0.15% arabinose, 5.5, 7, and 9 nM HSL with 0.2% arabinose) with or without 10 ng/mL aTc at 0.00004 OD and incubated at 37°C with shaking. Additionally, the open-loop was also induced with 0.2% arabinose and 0 nM HSL to match the unperturbed output fluorescence of the closed-loop in 0.2% and 7 nM HSL. At 4.5 hours, each culture was diluted into fresh matching prewarmed induction media with the same inducers at 0.00002 OD. At 9 hours, three 200  $\mu$ L aliquots of culture were col-

lected and measured by flow cytometry and the average of the technical replicates was used. The OD of the cultures were read at time 0 h, 4.5 h, and 9 h and used to estimate the growth rate for each culture. The reported data are from three independent biological replicates pooled from experiments performed on two separate days. For each biological replicate, a separate stock of media was independently prepared and used only for that particular replicate. Every biological replicate was started from its own independently-prepared overnight culture.

### Dynamic negative perturbation

5 mL aliquots of M9 media with appropriate antibiotics and 0.2% arabinose were inoculated with SKA703 pSKA417 pSKA562 (closed-loop) and SKA703 pSKA417 pSKA563 (open-loop) from glycerol freeze stocks at an OD of  $8 \times 10^{-8}$ . The cultures were incubated for 9 hours overnight at 37°C with shaking. In the morning, the overnight cultures were in early logarithmic phase. The overnight cultures were diluted into 5 mL fresh prewarmed induction media at 0.005 OD and incubated at 37°C with shaking. The overnight cultures were diluted into media containing 0.2% arabinose and 5.5 nM HSL. Every 1.5 hours, all cultures were rediluted into matching prewarmed induction media. At 4.5 hours, cells were at or close to steady-state (Time 0h in Fig. 2f). After 6 hours of incubation (Time 1.5h in Fig. 2f), each culture was diluted into two separate aliquots of medium and 10 ng/mL aTc was added to one aliquot and subsequent dilutions with these aTc-induced cultures were made with aTc-containing medium. At every dilution point, three 200  $\mu$ L samples of culture were collected and measured by flow cytometry and the average of the technical replicates were used. The reported data are from three independent biological replicates pooled

from experiments performed on two separate days. For each biological replicate, a separate stock of media was independently prepared and used only for that particular replicate. Every biological replicate was started from its own independently-prepared overnight culture.

## Growth rate control

### Growth rate titration

SKA1328 pSKA570 was grown overnight in M9 medium supplemented with 0.2% arabinose. Overnight culture was diluted 1:5,000 into 5 mL aliquots of methionine-dropout medium (M9 salts, 0.4% glucose, 0.001% thiamine, 20  $\mu\text{g}/\text{mL}$  uracil, 0.00006% ferric citrate, 0.1 mM calcium chloride, 1 mM magnesium sulfate, and 19 amino acids at 40  $\mu\text{g}/\text{mL}$ , methionine-free) containing 80 ng/mL methionine, 0.2% arabinose, and 10, 20, 30, or 40 nM HSL. Cultures were incubated at 37°C with shaking for twelve hours. Cultures were then diluted into fresh 5 mL aliquots of prewarmed dropout media with matching inducer concentrations at an OD of 0.0005. Immediately after dilution, 75  $\mu\text{L}$  samples were removed and mixed with 79  $\mu\text{L}$  of 500  $\mu\text{g}/\text{mL}$  rifampicin (Sigma-Aldrich Chemie GmbH) in phosphate-buffered saline and 21  $\mu\text{L}$  of 2  $\mu\text{m}$  AccuCount Blank Particles (Spherotech) in a 96-well plate (Greiner) on ice. Samples were collected every hour for nine hours. Absolute cell counts were determined by flow cytometry and used to calculate the actual cell concentration over time. An example of the gating strategy is presented in Extended Data Fig. 8d. Steady-state growth rate was calculated by taking the logarithm of the absolute cell counts and performing linear regression using a timepoint interval in which cells showed stable linear behavior (intervals indicated in the source data). The reported data are from three independent biologi-

cal replicates pooled from experiments performed on the same day. For each biological replicate, a separate stock of media was independently prepared and used only for that particular replicate. Every biological replicate was started from its own independently-prepared overnight culture.

### Robustness of growth rate control to different temperatures

SKA1328 pSKA570 (closed-loop) and SKA1328 pSKA571 (open-loop) were grown overnight in M9 medium with 0.2 % arabinose and appropriate antibiotics. Overnight cultures were diluted 1:5,000 into 5 mL aliquots of methionine-dropout medium (as described for growth rate titrations) containing 80 ng/mL methionine, 0.2% arabinose, 10 nM HSL, and appropriate antibiotics. Cultures were incubated at 37°C or 30°C with shaking for twelve hours to ensure that induced cells were in a state of active growth and that any residual methionine in the media was fully metabolized. Cultures were then diluted into fresh 5 mL aliquots of prewarmed dropout media (methionine-free) with matching inducer concentrations and antibiotics at an OD of 0.0005 for 37°C cultures or 0.001 for 30°C cultures. The 37°C cultures were started at a lower OD than the 30°C cultures in order to be able to follow the 37°C cultures over the duration of the experiment without the cells growing out of early exponential phase. Immediately after dilution, 75  $\mu\text{L}$  samples were removed and mixed with 79  $\mu\text{L}$  of 500  $\mu\text{g}/\text{mL}$  rifampicin (Sigma-Aldrich Chemie GmbH) in phosphate-buffered saline and 21  $\mu\text{L}$  of 2  $\mu\text{m}$  AccuCount Blank Particles (Spherotech) in a 96-well plate (Greiner) on ice. Samples were collected every hour for twelve hours. Absolute cell counts were determined by flow cytometry and used to calculate



the actual cell concentration over time. An example of the gating strategy is presented in Extended Data Fig. 8d. Steady-state growth rate was calculated by taking the logarithm of the absolute cell counts and performing linear regression as described above for Growth rate titrations. The reported data are from three independent biological replicates pooled from experiments performed on two separate days. For each biological replicate, a separate stock of media was independently prepared and used only for that particular replicate. Every biological replicate was started from its own independently-prepared overnight culture.

In an effort to match the growth rate of the closed-loop at 37°C, SKA1328 containing reduced plasmid copy number open-loop circuit pSKA571-p15A was used. To minimize the growth rate of the open-loop, it was decided not to induce the open-loop with HSL as the leaky expression of *metE* was sufficient. Growth rate control experiments were performed with 0.2% arabinose and 0 nM HSL. Dilutions, sampling, and growth rate calculations were performed as described above for Growth rate titrations. The reported data are from three independent biological replicates pooled from experiments performed on two separate days. For each biological replicate, a separate stock of media was independently prepared and used only for that particular replicate. Every biological replicate was started from its own independently-prepared overnight culture.

As a reference for the closed- and open-loop growth rate control circuits, endogenous *metE+* wild-type strain SKA703 with empty plasmid vector pSKA47 was also tested as described above with modifications to account for faster growth. The strain was grown overnight in M9 medium with 0.2 % arabinose and appropriate antibiotics. Overnight cultures were diluted 1:100,000 or 1:50,000 into 5 mL aliquots of methionine-dropout

medium (as described for growth rate titrations) containing 80 ng/mL methionine, 0.2% arabinose, 10 nM HSL, and appropriate antibiotics. The 1:100,000 dilutions were incubated at 37°C and the 1:50,000 dilutions were incubated at 30°C with shaking for twelve hours. Cultures were then diluted into fresh 5 mL aliquots of prewarmed dropout media (methionine-free) with matching inducer concentrations and antibiotics at an OD of 0.0001 for 37°C cultures or 0.0002 for 30°C cultures. Cultures were sampled as described above every 30 minutes for up to eight hours. 37°C cultures were terminated at 6.5 hours as they grew out of early exponential phase. Growth rate calculations were performed as described above for Growth rate titrations. The reported data are three independent biological replicates pooled from experiments performed on two separate days. For each biological replicate, a separate stock of media was independently prepared and used only for that particular replicate. Every biological replicate was started from its own independently-prepared overnight culture.

## Flow cytometry

The samples from the high throughput titrations in 96-well plates were analyzed on a LSRII Fortessa flow cytometer (BD Biosciences) equipped with the FACSDiva 8.0.1 software program and a high throughput sampler. sfGFP was measured with a 488 nm laser and 530/30 and 505 LP emission filters; the voltage gains of the instrument were set as follows: forward scatter 500 V, side scatter 300 V, SfgFP 900 V. A minimum of 5,000 events were collected for each well using thresholds of 500 FSC-H and 500 SSC-H.

Fluorescence measurements for the immunoblot lysate preparation cultures, step responses, steady-state negative perturbation, dynamic perturbation, and abso-

lute cell count measurements for the growth rate control experiments were performed using a CytoFlex S flow cytometer (Beckman Coulter) equipped with CytExpert 2.1.092 software. sfGFP was measured with a 488 nm laser and 525/40 BP filter; the gain settings of the instrument were as follows: forward scatter 100, side scatter 100, sfGFP 500. Thresholds of 2,500 FSC-H and 1,000 SSC-H were used for all samples. 50,000 events were collected for the lysate preparation, step response experiments, steady-state disturbance rejection experiments, and dynamic perturbation experiments and 1,000 AccuCount Blank Particles were collected for the growth rate control experiments.

The raw flow cytometry data was gated with FlowJo 10 (Treestar) (Extended Data Fig. 3a and 8d) and cell autofluorescence was subtracted from sfGFP measurements. The data was then further processed using custom R 3.5.0 scripts or plotted with GraphPad Prism 7. Background fluorescence is plotted in Extended Data Figure 3b. Excel was used to perform t-tests (unpaired, two-tailed, unequal variance).

## Data Availability

All relevant data are included as source data and/or are available from the corresponding author on reasonable request. Plasmid sequences are deposited in GenBank under the accession codes MK775703-MK775710. Strains and plasmids used in this study are available from the corresponding author on reasonable request.

## Code availability

Code used for simulations is available on reasonable request from the corresponding author.

## Extended Data Fig. Legends

**Extended Data Fig. 1. Deterministic modeling of the non-ideal antithetic integral feedback (AIF) circuit.** (a) Deterministic model of the non-ideal antithetic integral feedback circuit. (b,c) Output steady state and steady-state error for the non-ideal AIF circuit with dilution and negative disturbance. The black lines indicate curves of constant output steady state (nM) for a dilution rate corresponding to a typical bacterial growth rate. The green, blue and yellow shadings denote the regions of the parameter space in which the relative output steady-state error is less than 5% for dilution rates corresponding to typical values for bacteria, yeast and mammalian cells respectively.  $k = 0.037 \text{ min}^{-1}$  in (b) and  $3.85 \text{ min}^{-1}$  in (c). (d) Output steady state and steady-state error for the non-ideal AIF circuit with dilution, negative disturbance and actuator saturation. The black lines indicate curves of constant output steady state (nM) for a dilution rate corresponding to a typical bacterial growth rate. The green, blue and yellow shadings denote the regions of the parameter space in which the relative output steady-state error is less than 5% for dilution rates corresponding to typical values for bacteria, yeast and mammalian cells respectively. In this plot  $k = 1 \text{ min}^{-1}$ .

**Extended Data Fig. 2. Dependency of the adaptation region of the non-ideal AIF circuit with dilution, negative disturbance and saturation on the actuator gain  $k$ .** The black

curve has constant steady-state of 10000 nM for a dilution rate corresponding to a typical bacterial growth rate. The green shading shows the region of the parameter space in which the relative output steady-state error is less than 5%.

Extended Data Fig. 3. Fluorescence distributions of dynamic closed-loop circuit response. (a) Example of gating strategy for flow cytometry fluorescence measurements. Cells are first gated manually from background noise using a FSC-H/SSC-H plot (left panel). The gated cells are then selected for singlets using a SSC-Width/SSC-H plot (right panel). The percentage of events within each gate is indicated. (b) sfGFP fluorescence distributions for the dynamic step-response experiment in Fig. 2d as a function of time. The vertical orange line represents the mean. The vertical dashed grey line represents the mean of the background distribution, which was obtained by measuring non-fluorescent SKA703 cells containing pSKA570 and pSKA417.

Extended Data Fig. 4. AIF circuit with sfGFP output does not affect cell growth rate. (a) Dynamic growth rates for closed-loop step-responses presented in Fig. 2d. Circles indicate the individual replicates ( $n = 3$ ) and the average of the points is fit with a cubic spline. Shaded regions indicate the s.d.. (b) Steady-state growth rates for closed- and open-loop circuits in Fig. 2e. Data show mean  $\pm$  s.d. ( $n = 3$ ). Circles indicate the individual replicates. (c) Dynamic growth rates for

closed- and open-loop circuits in Fig. 2f. Circles indicate the individual replicates ( $n = 3$ ) and the average of the points is fit with a cubic spline. Shaded regions indicate the s.d.

Extended Data Fig. 5. *mf*-Lon protease-mediated degradation of AraC and sfGFP is closely matched. Protein levels of V5-tagged AraC with a Pdt#3c degradation tag with and without aTc-induction of *mf*-Lon were compared to fluorescence levels of sfGFP with a Pdt#1 tag. (a) Mean sfGFP fluorescence of the cultures used for lysate preparation. sfGFP fluorescence normalized to the pre-disturbance level. Error bars denote standard deviation ( $n = 3$ ). Circles denote the individual replicates. (b) Means of V5-tagged AraC immunoblot band intensities normalized to total protein. Band intensity normalized to the pre-disturbance level. Error bars denote standard deviation ( $n = 3$ ). Circles denote the individual replicates. (c) Immunoblot. Left panel: Total protein on membrane post-transfer. Right panel: V5-AraC-Pdt#3c immunoblot. V5-AraC-Pdt#3c is indicated with an arrow. SKA703 was included as a no plasmid negative control (neg ctrl). For immunoblot source data, see Supplementary Figure 1. Data are representative of three independent experiments.

Extended Data Fig. 6. Output steady-state error of the AIF circuit. (a) Steady-state error simulations of the non-ideal AIF circuit with dilution, negative disturbance and actuator saturation from Extended Data Fig. 1d. The black lines indicate curves of constant

output steady state (nM) for a dilution rate corresponding to a typical bacterial growth rate. The green, blue and yellow shadings denote the regions of the parameter space in which the relative output steady-state error is less than 5% for dilution rates corresponding to bacteria, yeast and mammalian cells respectively. In this plot  $k = 1 \text{ min}^{-1}$ . (b) Non-normalized output steady-states of closed- and open-loop circuits *in vivo* in the presence of *mf*-Lon protease perturbation from Fig. 2e and four additional HSL and ARA conditions. Data show mean  $\pm$  s.d. for  $n = 3$  independent biological replicates (gray circles). Two-tailed, unpaired, unequal variance t-test. (c) Heatmap of the steady-state error for the closed-loop and open-loop data presented in (b). (d) Matched output steady-states of the closed-loop circuit with 0.2% ARA and 7 nM HSL and the open-loop circuit with 0.2% ARA and 0 nM HSL. Data show mean  $\pm$  s.d. for  $n = 3$  independent biological replicates (gray circles). Two-tailed, unpaired, unequal variance t-test. (e) Fluorescence distributions for the closed- and open-loop circuits in (b). Data are representative of three independent experiments. (f) Non-normalized output for the closed- and open-loop dynamic disturbance rejection experiment presented in Fig. 2f. Mean sfGFP is plotted as a function of time and fit with a cubic spline for  $n = 3$  independent biological replicates. Shaded regions indicate the s.d.

Extended Data Fig. 7. Application of a negative perturbation reduces the output variance of closed-loop and open-loop cir-

cuits. sfGFP fluorescence variance for the closed-loop and open-loop circuits in Fig. 2e. Data show mean  $\pm$  s.d. for  $n = 3$  independent biological replicates (gray circles).

Extended Data Fig. 8. Additional growth rate control data. (a) Non-normalized growth rate data for the closed- and open-loop growth rate control circuits in Fig. 4d induced with 0.2% ARA and 10 nM HSL, an open-loop growth rate control circuit with reduced plasmid copy number (pSKA571-p15A, Open-loop (p15A)) induced with 0.2% ARA and 0 nM HSL, and a *metE+* wild-type strain (SKA703, wild-type) containing an empty plasmid vector induced with 0.2% ARA and 10 nM HSL. Closed- and open-loop circuits were placed in a  $\Delta metE$  host strain for testing. All strains were grown in methionine-free medium at 37°C and 30°C and steady-state growth rates were determined. Data show mean  $\pm$  s.d. for  $n = 3$  independent biological replicates (gray circles). Two-tailed, unpaired, unequal variance t-test. (b) Cell concentration plotted over time for the closed-loop circuit (closed circles), the open-loop circuit (open circles), and the reduced plasmid copy open-loop circuit (pSKA571-p15A, open triangles) in (a) and Fig. 3d. Gray circles indicate the individual replicates ( $n = 3$ ) and the average of the points is fit with a cubic spline. Error bars indicate the s.d. (c) Cell concentration plotted over time for the wild-type strain in (a). Gray circles indicate  $n = 3$  independent biological replicates and the average of the points is fit with a cubic spline. Error bars indicate the s.d. (d) Example of gating

strategy for absolute cell counts. Cells and beads are gated manually from background noise using a FSC-H/SSC-H plot (upper panel). The bead population can be seen in a magnified view (lower panel). The percentage of events within each gate is indicated.

Extended Data Fig. 9. Plasmids used in this study to construct host strain SKA703. (a) Suicide plasmids used to delete the arabinose, lactose, and rhamnose metabolic pathways from MG1655. The disrupted gene region as well as flanking upstream and downstream genomic sequences were inserted into suicide vector pRE112. The remaining deletion scar is indicated in red. (b)  $\lambda$ -integration plasmid used for the chromosomal integration of constitutively-expressed *lacYA177C*. (c) *Tn7*-integration plasmid used for the chromosomal integration of constitutively-expressed *tetR*.

Extended Data Fig. 10. Circuit plasmids used in this study. (a) *mf-lon* perturbation plasmid. (b) Synthetic circuit precursor plasmids. (c) Closed- and open-loop plasmids. (d) Closed- and open-loop growth rate control plasmids.